remote sensing

MDPI

Article

Post-Earthquake Damage Inspection of Wood-Frame Buildings by a Polarimetric GB-SAR System

Hai Liu [1], Christian Koyama [2], Jinfeng Zhu [1,*], Qinghuo Liu [3] and Motoyuki Sato [2,*]

[1] Department of Electronic Science, Institute of Electromagnetics and Acoustics, Xiamen University, Xiamen 361005, China; liuhai8619@xmu.edu.cn

[2] Center for Northeast Asian Studies, Tohoku University, Sendai 980-8576, Japan; christian.koyama@cneas.tohoku.ac.jp

[3] Department of Electrical and Computer Engineering, Duke University, Durham, NC 27708-0291, USA; qhl@duke.edu

* Correspondence: nanoantenna@hotmail.com (J.Z.); sato@cneas.tohoku.ac.jp (M.S.); Tel.: +81-22-795-6074 (M.S.)

Academic Editors: Salvatore Stramondo, Nicola Masini, Xiaofeng Li and Prasad S. Thenkabail
Received: 14 September 2016; Accepted: 3 November 2016; Published: 10 November 2016

Abstract: Structural damage inspection after an earthquake is essential for safety assessment of the affected wood-frame buildings and for making knowledgeable decision regarding their repair, renovation, or replacement. We present a polarimetric radar system for sensing the concealed wood-frames damaged by earthquakes. This system employs an antenna array consisting of four linearly polarized Vivaldi antennas recording full-polarimetric radar echoes in an ultra-wideband ranging from 1 to 20 GHz. The detailed design of the system and the signal processing algorithms for high-resolution 3D imaging are introduced. We conducted a number of surveys on damaged wooden wall specimens in laboratory. The experiment results indicate that the high-frequency radar waves can penetrate the wooden walls. Deformations of wooden structures (about 2 cm displacement) inside the wall, as well as the concealed small metal nails (about 3 mm in diameter and less than 2 cm in length) and bolts can be clearly imaged. The shape and orientation of the wooden members have shown a great sensitivity to the radar polarization. It is concluded that radar polarimetry can provide much richer information on the condition of concealed building structures than the conventional single-polarization subsurface penetrating radar.

Keywords: ground-based synthetic aperture radar (GB-SAR); radar polarimetry; wood-frame building; earthquake damage; non-destructive testing (NDT)

1. Introduction

Destructive earthquakes cause different degrees of damage to buildings all over the world each year. The rate of collapsed buildings, the grade of damage in the affected area, and the types of damages to each building are essential information for successful rescue and reconstruction in the disaster area [1,2]. In the stage of post-earthquake reconstruction, there is a great demand for efficient and accurate assessment of the safety of in situ residential buildings. Recently, space-borne and air-borne remote sensing techniques, including optical sensors [3] and synthetic aperture radar (SAR) [4,5], have been popularly used for the overall damage evaluation in a vast area. These remote sensing techniques can detect collapsed or obviously unsafe buildings. For the moderately and/or slightly damaged buildings, visual observation by experienced engineers is still the main method to evaluate their safety [6,7]. However, a visual inspection is restricted to check the superficial damages—e.g., crack, spalling, deformation, etc.—and the evaluation results highly depend on the engineer's experience. To deal with concealed earthquake damage, invasive techniques based on drilling have been popularly

applied [8]. To avoid the secondary damage to building structures, many non-destructive testing (NDT) methods have been developed for inspection and evaluation of earthquake-induced structural damages [9]. Stress wave measurements—which include elastic, acoustic, and ultrasonic waves—can identify the internal deterioration [10] and crack [11], and can determine the mechanical properties of a structural member, such as modulus of elasticity and strength. While the stress wave measurements require the access to both sides of the structural member. Acoustic emission measurement has been used to predict earthquake damage in a concrete core under uniaxial compressive loading [12], and to detect biodegradation in wooden buildings [13].

Wood-frame residential buildings are popularly constructed in earthquake-prone countries, due to its good seismic performance [14]. For instance, over two million housing units are built annually in North America and Japan. The general range of the fraction of wood structures to total structures seems to be between 80% and 90% in all regions of the USA [15]. Recently, wood-frame construction is not only used for single- and multi-family dwellings, but also for low-rise commercial and industrial buildings [16]. Unlike steel or concrete structures, earthquake damage to wood-frame buildings cannot be readily observed by naked eyes, since wooden structures are commonly covered by wall finishes made of gypsum or other materials. Thus, development of NDT techniques without removal of wall finishes is of significant meaning for damage inspection of the invisible wooden structures. Thermography, X-ray radiography, nuclear magnetic resonance, and radar imaging have been tentatively studied [17,18]. Among these techniques, radar imaging is one of the most promising approaches, because it allows for quick data acquisition and imaging of non-accessible structures inside the wall. In addition, polarimetric radar can provide richer information of embedded and/or buried objects [19], and can enhance the diagnostic power required for building inspection [20,21]. Up to now, the major limitation of microwave sensing techniques for the real use of inspecting wooden structures is its insufficient resolution for detecting small defects inside a damaged wooden structure, of which the common types are cracks, loosening or failing of connections, large deformation, etc. [14].

To detect the subsurface damage of the wooden structure with sufficient resolution, we developed a ground-based synthetic aperture radar (GB-SAR) system operating in an ultra-wideband (UWB) from 1 to 20 GHz. The image resolution can be greatly improved as a result of the UWB operation and SAR processing. In addition, the full-polarimetric data analysis can provide complementary information on the targets. The rest of this paper is organized as follows. The second section presents the damaged wood wall specimens, the developed polarimetric GB-SAR system and the signal processing algorithms. The third section shows the laboratory experiment results, and is followed by the discussions and conclusions.

2. Materials and Methods

2.1. Wall Specimen of Damaged Wooden Structure

In most wood-frame structures, wood shear walls are the primary structural element that resists lateral earthquake loads. Therefore, we test two types of wooden walls, which are commonly used to construct private residential houses in Japan. Their designs are shown in Figure 1. We manufactured two specimens for each type, one of which was damaged by pressing a jack until the inner wood structure lost its bearing capacity.

Type II walls were designed in Japan after 1981, when an improved regulation for wood-frame residential buildings was issued. This design features a diagonal brace, which joints the post and beam with metal clamps and plates. This brace is mainly used to resist the horizontal earthquake vibration, as shown in Figure 1b. A decorating plywood board covers on the interior side of the wall and a corrugated steel sheet covers the exterior side. Glass wool is filled inside the wall for heat-isolation.

The Hanshin-Awaji earthquake occurred in 1995 and then the regulation was again renewed. Figure 1a shows another design of wooden wall, namely type I, which have been commonly used in Japan after 1995. This design consists of vertical posts and horizontal beams. Metal bolts inside

the wood members are used to join the posts and beams. A 12.5 mm thick gypsum board is mounted on the interior side of the wall. On the exterior side, a 14 mm thick ceramic board and a 9 mm thick structural plywood board are mounted. The resistance to earthquake shaking is mainly provided by the plywood board, which is fixed on the wood structure using a number of small steal nails, as illustrated in Figure 1a. The size of the nails is about 3 mm in diameter and less than 2 cm in length. Inside the wall, styrofoam is filled for heat-isolation.

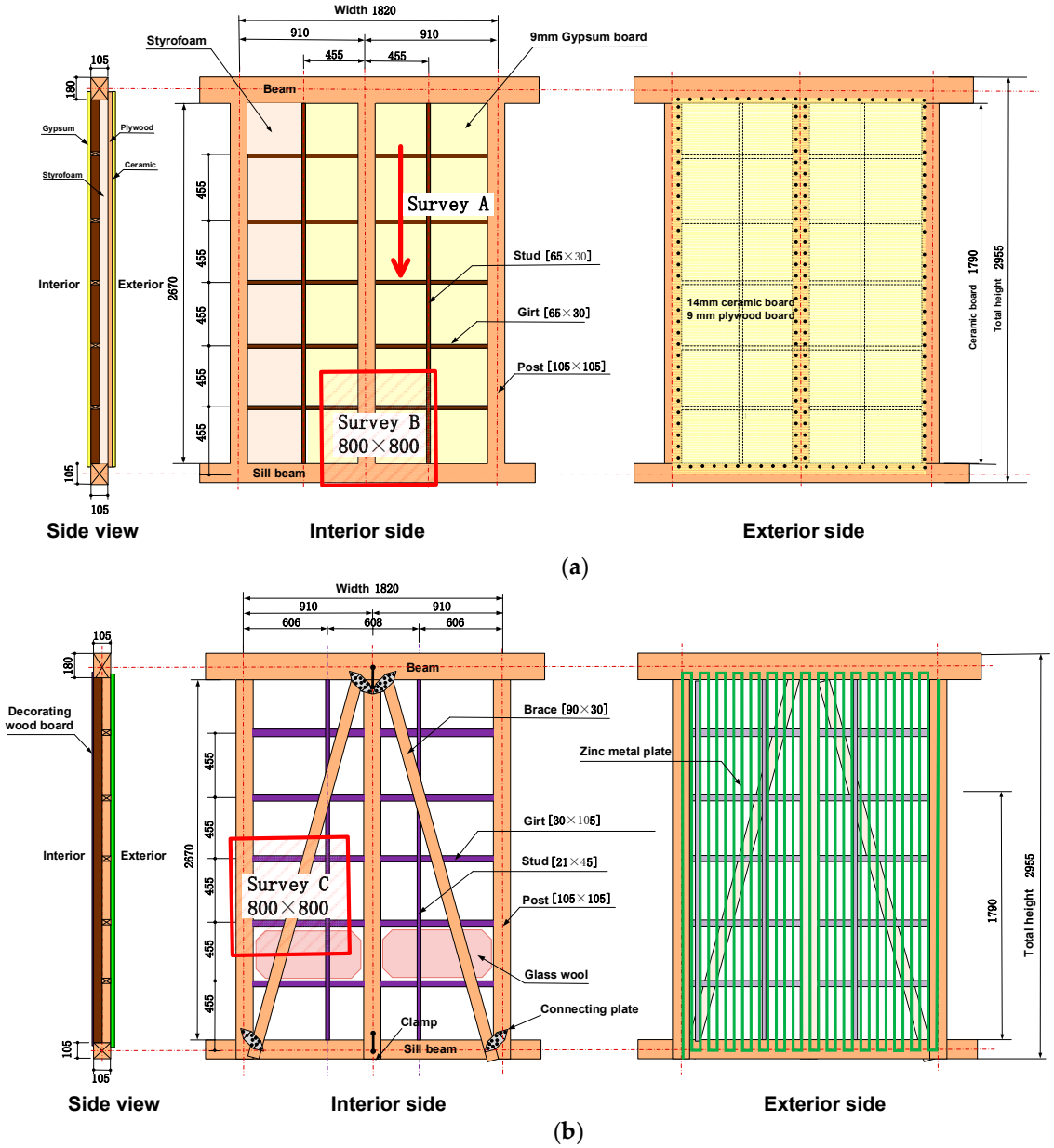

Figure 1. Designs of sample wooden walls. (**a**) Type I; (**b**) Type II. One survey line and two survey areas are marked by red color. The unit is in millimeter.

2.2. Polarimetric GB-SAR System

A Vivaldi antenna with a size of 7.5 cm in width and 7.8 cm in height is employed to configure a polarimetric antenna array (Figure 2). Theoretically, this Vivaldi antenna can transmit/receive linearly polarized electromagnetic waves, and operates over an unlimited frequency band above its lower cut-off frequency of about 1 GHz, which is determined by its opening width. This traveling-wave

antenna has a favorable waveform in the time domain [22]. The polarimetric antenna array consists of four Vivaldi antennas, of which two are horizontally (H-channel) and the other two are vertically (V-channel) oriented. The spacing between them is 9.5 cm as shown in Figure 2. By switching the combinations of two active antennas as a pair of transmitting and receiving sensors, we can acquire a full-polarimetric dataset—i.e., in HH, HV, VH, and VV polarizations, respectively.

We have set up a stepped frequency GB-SAR system based on a four-port vector network analyzer (VNA), as shown in Figure 3. The polarimetric antenna array is mounted to a 2D positioning system. The movement of the antenna and the data acquisition are synchronized by a measuring program in a PC. The main measurement parameters are given in Table 1. 801 frequency samples are recorded over the range from 1 to 20 GHz with a frequency step of 23.75 MHz. The antennas are connected to the four-channel VNA by coaxial cables. A full-polarimetric dataset can be simultaneously recorded at each sampling position. The dimension of the positioning system is 1.5 m by 1.5 m. This system moves the antenna in both x and y directions. The maximum movement range of the antenna array is about 1 m in both directions, due to the spatial limitation.

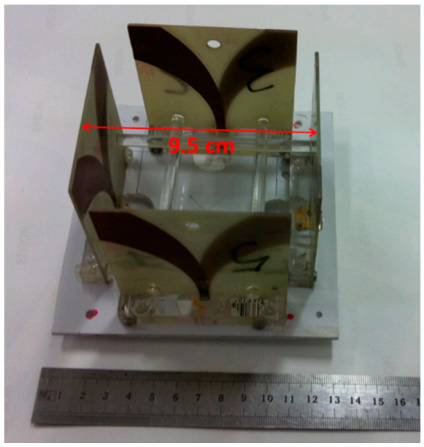

Figure 2. Polarimetric antenna array consisting of four Vivaldi antennas.

Figure 3. Developed polarimetric GB-SAR system. The line with an arrow indicates the position of the 1D survey line in Figure 1a.

Table 1. Measurement parameters of the GB-SAR system.

Frequency Range	1 GHz–20 GHz
Polarimetric Combination	HH/HV/VH/VV
Antenna Moving Step	5 mm
Scan Area	80 cm × 80 cm

2.3. Signal Processing

The signal processing procedure mainly consists of pulse compression, antenna phase center calibration, SAR processing, and polarimetric imaging.

2.3.1. Pulse Compression

A ringing component (time sidelobes) trailing the radiated wavelet can commonly be observed due to the antenna resonance, which extends the impulse response of the antenna, and degrades the range resolution. To suppress the antenna ringing and compress the transmitted pulse, we apply a deconvolution technique using a Wiener filter, which is an optimal tradeoff between an inverse filter and a matched filter. The Wiener filter is executed in the frequency domain [23], and expressed as

$$Y(\omega) = \frac{X(\omega)H^*(\omega)}{|H(\omega)|^2 + \beta}, \tag{1}$$

where $H(\omega)$, $X(\omega)$, $Y(\omega)$, β, and ω are respectively the reference wavelet, the input signal, the output signal, a regularization parameter and the angular frequency, and the superscript (*) denotes the complex conjugate. The value of the regularization parameter determines the performance of the Wiener filter, which becomes an inverse filter when β is zero, and changes to a matched filter when β is infinity.

The reference wavelet is obtained from a time-gated transmission signal, which is recorded with two Vivaldi antennas placed face-to-face at a separation of 0.5 m. A tapered time gating is applied to exclude the reflected and/or diffracted signal from the surroundings. The regularization parameter is determined by the signal-to-noise ratio. By testing, we determined the regularization parameter in our data processing as 10 percent of the mean power of the whole spectrum of the recorded reference wavelet. By applying the Wiener filtering, we can clearly discern that the ringing component of the transmitted wavelet has been suppressed and the source spectrum is broadened (data not shown).

2.3.2. Antenna Phase Center Calibration

After a standard VNA calibration, the reference plane, i.e., the time-zero position, is located at the antenna feeding point. However, the electromagnetic waves are radiated from an apparent reference point—i.e., antenna phase center [22]. For a Vivaldi antenna, the phase center is located neither at its feeding point nor at its aperture center, but between them on its symmetric axis, as illustrated in Figure 4. The precise knowledge of the location of the antenna phase center is important for the accurate ranging. Moreover, it is also significant for SAR processing, because it accurately simplifies an antenna as a point source [24].

We used a multi-offset transmission measurement for locating the apparent phase center position. The details of the method and the experiment procedure are described in [24]. The phase center position of the Vivaldi antenna is estimated to be located 2.0 cm away from the antenna aperture towards the antenna feeding point. Meanwhile, the time delay at the estimated phase center relative to the feeding point is estimated to be 0.4 ns. This antenna delay is corrected and the physical antennas are simplified to be point sources in the following SAR processing.

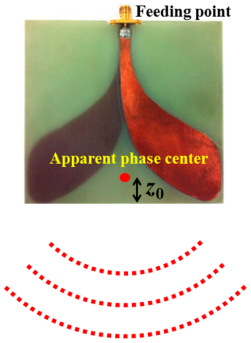

Figure 4. The apparent antenna phase center. The dotted curves denote wavefront radiated from the apparent phase center at three different range distances.

2.3.3. Bistatic SAR Processing

One of the common SAR (migration) processing algorithms in time domain, namely back propagation, is applied to collapse the hyperbolic diffraction and to increase the azimuth resolution. Our targets are in the near range, relative to the dominant wavelength and the antenna separation. Therefore, we adopt a bistatic model for the SAR processing algorithm, as shown in Figure 5. The antennas are simplified as point sources suspending at a height of z_a from the ground surface. The algorithm is expressed as

$$S_{out}(x,y,z) = \sum_{i=1}^{M}\sum_{j=1}^{N} S_{in}(x_{i,j}, y_{i,j}, (r_1 + r_2)/v), \tag{2}$$

where S_{in} is the acquired raw data, $S_{out}$is the reconstructed image, r_1 is the ray path from the apparent phase center of the transmitting antenna at $(x_{i,j}, y_{i,j}, z_a)$ to the imaging point at (x, y, z), r_2 is the ray path from the imaging point back to the apparent phase center of the receiving antenna at $(x_{i,j} + d, y_{i,j}, z_a)$, d is the antenna separation, v is the propagation velocity of electromagnetic waves, M and N are the number of measurement points in x and y directions, respectively. Most of the volume inside the wall is occupied by heat-isolation material, whose dielectric properties are close to those of air. Thus, we ignore the velocity variation of electromagnetic waves in air, wood, and other media, and use the speed of light in the SAR processing. The expressions of r_1 and r_2 are given by

$$r_1 = \sqrt{(x_{i,j} - x)^2 + (y_{i,j} - y)^2 + (z_a + z)^2} \tag{3}$$

$$r_2 = \sqrt{(x_{i,j} + d - x)^2 + (y_{i,j} - y)^2 + (z_a + z)^2} \tag{4}$$

where z_a is the height of the apparent antenna phase center above the surface of wooden wall under investigation.

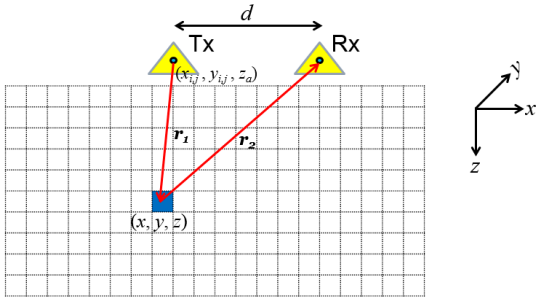

Figure 5. Geometry of the bistatic model for the SAR processing.

2.3.4. Polarimetric Imaging

After the SAR processing, we obtain a reconstructed image in each polarization channel. The full polarimetric information can be represented in a 2×2 scattering matrix $[S]$ [25], which is given by

$$[S] = \begin{bmatrix} S_{HH} & S_{HV} \\ S_{VH} & S_{VV} \end{bmatrix} \quad (5)$$

To view the combined contribution from different polarization channels, a RGB image can be generated presenting the full polarimetric information with the intensities of the Pauli decomposed components: $|S_{HH} - S_{VV}|$, $|S_{HH} + S_{VV}|$ and $2|S_{HV}|$, which are color-coded in the red, blue, and green channels, respectively. From the resulting polarimetric image, we can obtain more information on the targets by analyzing the scattering mechanism.

3. Results

A number of non-contact measurements were conducted by the developed GB-SAR system on the wood wall specimens to check the system performance and to image the concealed damage to the wood structures. This section presents the results of a 1D survey and two 2D surveys on those two damaged wall samples.

3.1. Survey A

To evaluate the penetration of electromagnetic waves through the wood wall in the frequency range up to 20 GHz, we firstly carried out a 1D survey on the Type I wall, as shown in Figure 1a. The survey line is also indicated by a line with an arrow in the photo in Figure 3. Note that, due to height limitation of the experiment room, the wall specimen has been rotated anticlockwise by 90 degrees. Figure 6 shows the acquired raw radar profile in the VV polarization. At the depth of around 40 cm and y position of 0.5 m, we can see a distinct hyperbolic reflection stemming from a supporting steel pipe behind the wall. This verifies that the high-frequency electromagnetic waves have sufficient penetration through the wooden walls, which are dry and impose low attenuation to electromagnetic waves. Above the steel pipe reflection, we can also discern two clear reflections at the depths of 5 cm and 15 cm, which come from the top and bottom of the embedded wooden girts. Besides these, two horizontal reflections from the interior and exterior covering boards are also observed. Nevertheless, due to the wave scattering, the raw radar profile cannot provide a good lateral resolution to identify the damage.

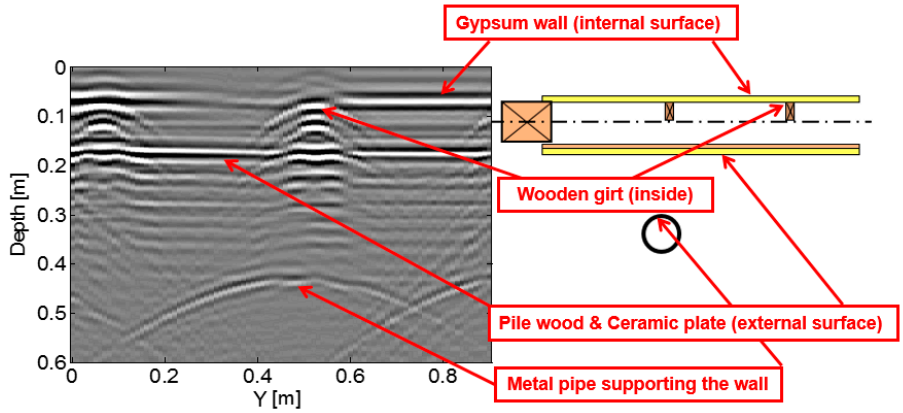

Figure 6. Raw radar profile acquired along the 1D survey line on the Type I wall specimen (Figures 1a and 3).

3.2. Survey B

A 2D survey was conducted on an 80 cm by 80 cm area on the Type I wall specimen, as shown in Figure 1a. The measurement step was 5 mm in both x and y directions. Figure 7 shows the reconstructed SAR images at a depth of 3.2 cm in three different polarization channels. After SAR processing, the reconstructed images provide much higher lateral resolution than the raw radar profile in Figure 6. Besides, different polarizations show different images of the same wood structure. The reflection from the vertical post (in y direction) is stronger than that from the horizontal girt in the VV polarization channel, while weaker in the HH polarization channel. In the HV polarization channel, we can also notice two small inclined linear reflections at the joint of the vertical post and the horizontal girt. These two reflections come from two connecting steel bolts inside the wooden members, which cannot be discerned even if we remove the decorating gypsum wall. On the wooden post and sill beam, especially in the reconstructed slices at a shallow depth, we can see some evenly aligned small reflections. These reflections come from the small nails fixing the gypsum wall on the wooden structure, and are clearer on the shallower reconstructed images (data not shown). The size of these nails is about 3 mm in diameter and less than 2 cm in length.

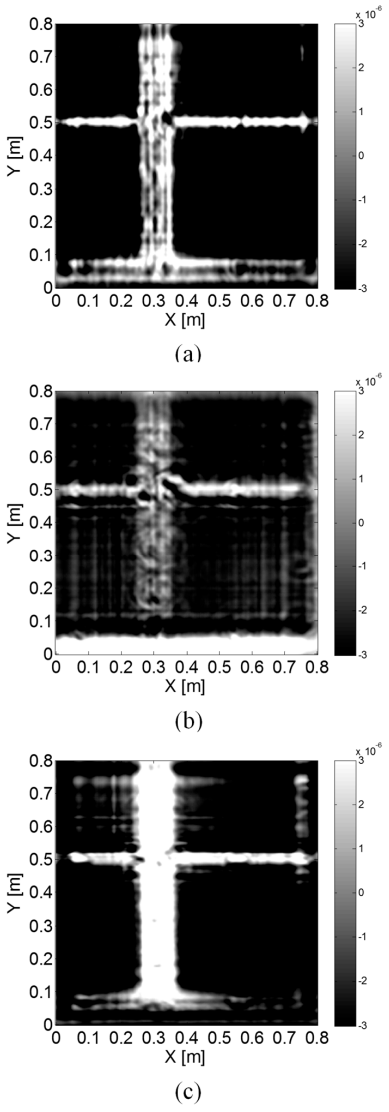

Figure 7. Reconstructed SAR image of the 2D survey on the Type I wall specimen (Figure 1a) in (**a**) HH; (**b**) HV; and (**c**) VV polarization channel.

3.3. Survey C

Another 2D survey was conducted on an 80 cm by 80 cm area on the Type II wall specimen, as shown in Figure 1b. Again, the measurement step was 5 mm in both directions. Figure 8 shows the reconstructed image at a depth of 2.3 cm in the HH polarization channel. The vertical post, horizontal girt, and the inclined brace are well imaged. Different from the post and girt, the inclined brace shows variable phase in a short section—i.e., bright at portions A and C while dark in the middle portion B. After the measurement, we removed the covering plywood board and a photo of the wooden structure under it is shown in Figure 9. We found that the inclined brace had been completely crushed. There are two opening cracks at parts A and C and a downward deflection of about 2 cm at part B. Therefore, the variable phase of the brace in Figure 8 is the electromagnetic response of the severe deformation of the brace after the crushing. The distance from the surface of the deformed wooden brace to the radar sensor varies along it. As a result, the time delay—i.e., phase of the reflected signal varies. However, the cracks on the top surface of portions A and C, as well as the crack on the bottom surface of portion B of the brace are hardly identifiable in the reconstructed images.

Figure 10 shows the Pauli-RGB image generated from the full polarimetric dataset after SAR processing in each polarization channel. Due to the fact that, in contrast to the conventional 2D SAR case, in the subsurface SAR case we are dealing with 3D imaging, we cannot simply apply a conventional interpretation of the Pauli color coding. Nevertheless, in the composite RGB image we can easily note the differences in scattering behavior between the damaged and undamaged parts. The intact post and girt show no obvious variations in their color representation. On the contrary, a significant variation can be observed for the diagonal wooden brace. The parts A and C of the brace show green colors, while the colors change into blue for the crushed part B in the middle. Also, the contributions of the reflections from the corrugated steel sheet on the bottom side are easy to identify in the color image.

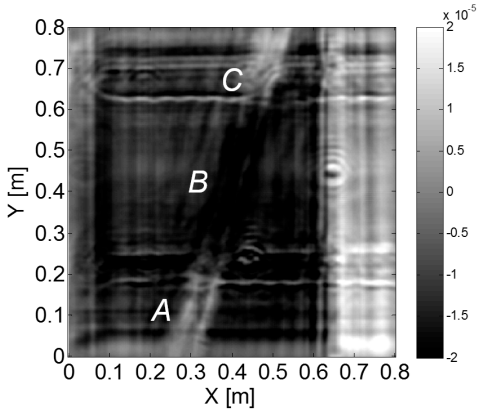

Figure 8. Reconstructed SAR image of the 2D survey on the Type II wall specimen in Figure 1b at a depth of 2.3 cm from the wall surface in HH polarization channel.

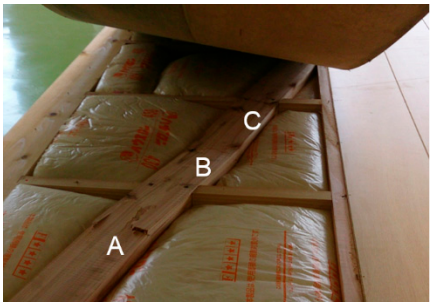

Figure 9. Photo of the deformed brace under the decorating wood board of specimen I.

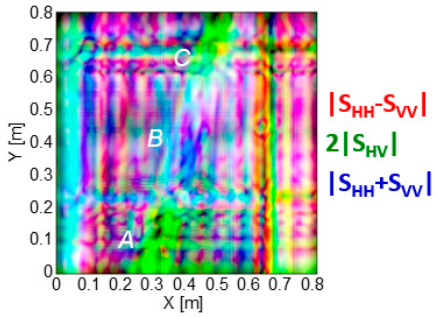

Figure 10. RGB image generated from the 2D survey on the Type II wall specimen in Figure 1b at a depth of 2.3 cm from the wall surface.

4. Discussions

4.1. Strengths and Limitations of This Work

As shown in Figure 7, radar polarimetry has shown a large sensitivity to the shape and orientation of the wooden members. Polarimetric radar technique is able to provide richer information than the conventional single-polarization subsurface penetrating radar. This has also been verified by M. Pieraccini et al., when they use radar polarimetry to detect the cavity embedded inside a masonry wall [20]. Moreover, radar polarimetry can suppress clutter and enhance the target signal [26]. We have not conducted a polarimetric calibration to the developed polarimetric GB-SAR system, since the polarimetric calibration over a ultra-wideband is extremely challenging [27]. This limits the accurate analysis of the polarimetric signature from the RGB Pauli image in Figure 10. Further investigation would be carried out to fully explore the potential of radar polarimetry for quantitative interpretation of the earthquake damage to the wood-frame buildings in our future work.

The survey of the developed GB-SAR system is similar to a 3D survey of ground penetrating radar (GPR) [28]. The main superiority of the GB-SAR over a 3D GPR system is its high resolution, as a result of the employed UWB Vivaldi antenna. We have shown that the 3 mm metal nails can be detected by the UWB GB-SAR system. In contrast, the cracks shown in Figure 9 are hardly recognized. This is because the metal nail, as a perfect electric conductor, can reflect strong electromagnetic energy. While, the crack on the crushed brace in Figure 9 is less than 1 mm in aperture that its reflection is hardly detectable, since the reflection energy from a crack is proportional to its aperture size [29].

We have demonstrated that SAR processing can greatly improve the lateral resolution in the reconstructed image. Nevertheless, the lateral resolution would be degraded if we increase the distance from the antenna tip to the wall surface (z_a), due to the limited scan aperture of our GB-SAR system. Furthermore, less energy can be penetrated into the wooden wall as a result of wavefront spreading if we increase z_a. From these two points of view, the GB-SAR sensor has to work in its near range.

4.2. Feasibility and Further Improvements

To judge whether a building is safe to enter and reoccupy is of great concern after a disastrous earthquake. Compared with buildings made of concrete materials, wood-frame buildings have received little attention from the perspective of damage inspection and evaluation. Although the presented technique can help a civil engineer see the wooden structures through the covering wall finishes, it can only be used as a supplement, rather than a substitution of the visual inspection [7].

Further research efforts from three aspects should be poured to improve the developed GB-SAR system and the imaging algorithm. Firstly, the current GB-SAR system, based on a 2D scanner and a VNA, works in an inefficient way and the 80 cm $\times$ 80 cm survey consumes more than eight hours. This is impractical for field applications. Development of a multi-input multi-output (MIMO) antenna array system would be desired. A MIMO array can acquire 3D data over a swath by a single scan and meets the survey speed requirement [30]. Secondly, the variation of electromagnetic wave propagation

velocity in wood, air, and other media has not been considered in the SAR processing. A reverse time migration (RTM) algorithm [31], which can incorporate a detailed dielectric model of the wooden wall based on the design, should be investigated in the future. Thirdly, besides Pauli decomposition, other polarimetric representation methods—e.g., alpha-entropy decomposition [25] and Yamaguchi four-component decomposition [32]—should be tested to further explore the quantitative information of the damaged wooden structures from the polarimetric GB-SAR dataset.

5. Conclusions

In this paper, we present a polarimetric GB-SAR system for non-destructive imaging and inspection of wooden structures damaged by earthquakes. SAR processing has been applied to improve the lateral resolution of the reconstructed radar image. The results from our laboratory experiments demonstrate that the high-frequency radar waves can penetrate the wooden walls. Deformations of the wooden structures, as well as the concealed metal nails (about 3 mm in diameter and less than 2 cm in length) and bolts inside the walls can be clearly imaged. The subtle crack (less than 1 mm in aperture) on the wooden members cannot be identified due to its weak reflection and limited resolution. The shape and orientation of the wooden members have shown a great sensitivity to radar polarization. It is concluded that radar polarimetry can provide much richer information on the condition of the concealed building structures than the conventional single-polarization subsurface penetrating radar. The rather complex subsurface scattering mechanisms inside a wood wall will be subject to further investigation to fully understand the information.

Acknowledgments: This work is partly supported by National Natural Science Foundation of China (41504111). The research results have been achieved by "Development of Non-Destructive Inspection Method for Constructions by Electromagnetic Wave", the Commissioned Research of National Institute of Information and Communications Technology (NICT), Japan.

Author Contributions: Hai Liu and Motoyuki Sato conceived and designed the experiments; Hai Liu and Christian Koyama performed the laboratory experiments; Jinfeng Zhu and Qinghuo Liu processed and analyzed the datasets, Hai Liu drafted the manuscript, which was revised and approved by all the authors.

Conflicts of Interest: The authors declare no conflict of interest.

References

1. Dong, L.; Shan, J. A comprehensive review of earthquake-induced building damage detection with remote sensing techniques. *ISPRS J. Photogramm. Remote Sens.* **2013**, *84*, 85–99. [CrossRef]
2. Schweier, C.; Markus, M. Classification of collapsed buildings for fast damage and loss assessment. *Bull. Earthq. Eng.* **2006**, *4*, 177–192. [CrossRef]
3. Vetrivel, A.; Gerke, M.; Kerle, N.; Vosselman, G. Identification of structurally damaged areas in airborne oblique images using a visual-bag-of-words approach. *Remote Sens.* **2016**, *8*, 231. [CrossRef]
4. Sato, M.; Chen, S.-W.; Satake, M. Polarimetric SAR analysis of tsunami damage following the March 11, 2011 East Japan earthquake. *Proc. IEEE* **2012**, *100*, 2861–2875. [CrossRef]
5. Zhai, W.; Shen, H.; Huang, C.; Pei, W. Building earthquake damage information extraction from a single post-earthquake PolSAR image. *Remote Sens.* **2016**, *8*, 171. [CrossRef]
6. Meada, M.; Kang, D. Post-earthquake damage evaluation of RC buildings. *J. Adv. Concr. Technol.* **2009**, *7*, 327–335. [CrossRef]
7. Consortium of Universities for Research in Earthquake Engineering. *General Guidelines for the Assessment and Repair of Earthquake Damage in Residential Woodframe Buildings*; CUREE: Richmond, CA, USA, 2010.
8. Sousa, H.S.; Sørensen, J.D.; Kirkegaard, P.H.; Branco, J.M.; Lourenço, P.B. On the use of NDT data for reliability-based assessment of existing timber structures. *Eng. Struct.* **2013**, *56*, 298–311. [CrossRef]
9. Santos-Assuncao, S.; Perez-Gracia, V.; Caselles, O.; Clapes, J.; Salinas, V. Assessment of complex masonry structures with GPR compared to other non-destructive testing studies. *Remote Sens.* **2014**, *6*, 8220–8237. [CrossRef]
10. Suzuki, K.; Nagao, H. Deterioration diagnosis of wooden bridges by nondestructive testing method. *Wood Preserv.* **2005**, *31*, 12–19.

11. Yanagida, H.; Tamura, Y.; Kim, K.-M.; Lee, J.J. Development of ultrasonic time-of-flight computed tomography for hard wood with anisotropic acoustic property. *Janpanese J. Appl. Phys.* **2007**, *46*, 5321–5325. [CrossRef]
12. Suzuki, T.; Ohtsu, M. Damage estimation of concrete canal due to earthquake effects by acoustic emission method. *Constr. Build. Mater.* **2014**, *67*, 186–191. [CrossRef]
13. Fujii, Y.; Fujiwara, Y.; Kigawa, R.; Suda, T.; Suzuki, Y. Characteristics and diagnosing technology of biodegradation in wooden historical buildings a case study on Amida-do in Higashi Hongan-ji Temple in Kyoto. In Proceedings of the World Conference on Timber Engineering (WCTE2010), Riva del Garda, Italy, 20–24 June 2010; pp. 19–24.
14. Dogangun, A.; Tuluk, Ö.I.; Livaoglu, R.; Acar, R. Traditional wooden buildings and their damages during earthquakes in Turkey. *Eng. Fail. Anal.* **2006**, *13*, 981–996. [CrossRef]
15. Ayoub, A. Seismic analysis of wood building structures. *Eng. Struct.* **2007**, *29*, 213–223. [CrossRef]
16. Van de Lindt, J.W.; Gupta, R.; Pei, S.; Tachibana, K.; Araki, Y.; Rammer, D.; Isoda, H. Damage Assessment of a full-scale six-story wood-frame building following triaxial shake table tests. *J. Perform. Constr. Facil.* **2012**, *26*, 17–25. [CrossRef]
17. Bucur, V. Techniques for high resolution imaging of wood structure: A review. *Meas. Sci. Technol.* **2003**, *14*, R91–R98. [CrossRef]
18. Bucur, V. *Nondestructive Characterization and Imaging of Wood*; Springer: Berlin, Germany, 2003.
19. Feng, X.; Yu, Y.; Liu, C.; Fehler, M. Combination of H-Alpha decomposition and migration for enhancing subsurface target classification of GPR. *IEEE Trans. Geosci. Remote Sens.* **2015**, *53*, 4852–4861. [CrossRef]
20. Pieraccini, M.; Pisaneschi, M.; Noferini, L.; Atzeni, C. Polarimetric radar signature of masonry walls. *NDT E Int.* **2007**, *40*, 271–274. [CrossRef]
21. Martínez-Sala, R.; Rodríguez-Abad, I.; Diez Barra, R.; Capuz-Lladró, R. Assessment of the dielectric anisotropy in timber using the nondestructive GPR technique. *Constr. Build. Mater.* **2013**, *38*, 903–911. [CrossRef]
22. Balanis, C.A. *Antenna Theory: Analysis and Design*, 3rd ed.; Wiley-Interscience: New York, NY, USA, 2005.
23. Gaballah, M.; Sato, M. A new approach to enhancement of ground penetrating radar target signals by pulse compression. *Explor. Geophys.* **2009**, *40*, 77–84. [CrossRef]
24. Liu, H.; Sato, M. Determination of the phase center position and delay of a Vivaldi antenna. *IEICE Electron. Express* **2013**, *10*, 1–7. [CrossRef]
25. Lee, J.-S.; Pottier, E. Polarimetric radar imaging: From basics to applications. In *Optical Science and Engineering*; CRC Press: Boca Raton, FL, USA, 2009.
26. Moriyama, T.; Kasahara, H.; Yamaguchi, Y.; Yamada, H. Advanced polarimetric subsurface FM-CW radar. *IEEE Trans. Geosci. Remote Sens.* **1998**, *36*, 725–731. [CrossRef]
27. Feng, X.; Zou, L.; Lu, Q.; Liu, C.; Liang, W.; Zhou, Z.-S. Calibration with high-order terms of polarimetric GPR. *IEEE J. Sel. Top. Appl. Earth Obs. Remote Sens.* **2012**, *5*, 717–722. [CrossRef]
28. Núñez-Nieto, X.; Solla, M.; Novo, A.; Lorenzo, H. Three-dimensional ground-penetrating radar methodologies for the characterization and volumetric reconstruction of underground tunneling. *Comput. Chem. Eng.* **2014**, *71*, 551–560. [CrossRef]
29. Diamanti, N.; Redman, D. Field observations and numerical models of GPR response from vertical pavement cracks. *J. Appl. Geophys.* **2012**, *81*, 106–116. [CrossRef]
30. Liu, H.; Chen, J.; Zou, L.; Takahashi, K.; Sato, M. Development of an array GPR system for large-scale archaeological investigations. In Proceedings of the 11th SEGJ International Symposium, Yokohama, Japan, 18–21 November 2013; pp. 107–110.
31. Liu, H.; Zhang, Y.; Qiu, C.; Han, F.; Liu, Q.H. Reverse-time migration and full waveform inverson applied to a stationary MIMO GPR system. In Proceedings of the 2016 International Geoscience and Remote Sensing Symposium (IGARSS2016), Beijing, China, 2016; pp. 1–4.
32. Yamaguchi, Y.; Moriyama, T.; Ishido, M.; Yamada, H. Four-component scattering model for polarimetric SAR image decomposition. *IEEE Trans. Geosci. Remote Sens.* **2005**, *43*, 1699–1706. [CrossRef]